PCCP

ROYAL SOCIETY OF CHEMISTRY

PAPER

Published on 10 August 2026

Cite this: *Phys. Chem. Chem. Phys.*, 2026, **28**, 20893

Decoding orbital interactions in H-bonded melamine networks by combining electron spectroscopy and DFT

Iulia Emilia Brumboiu, *[a] Cesare Grazioli,[b] Matuš Stredansky, †[bc] Teng Zhang, ‡[d] Monica de Simone, [b] Marcello Coreno, [e] Carla Puglia, [d] Barbara Brena§[d] and Valeria Lanzilotto *[f]

The effects of hydrogen bonding (HB) on the electronic structure of melamine films are investigated by analyzing the electronic states of hydrogen-bonded aggregates in terms of the molecular orbitals (MOs) of the isolated monomer. This approach provides an orbital description of HB directly connected to the spectroscopic signatures observed in valence-level photoemission spectroscopy (VL-PES) and N 1s near edge X-ray absorption fine structure spectroscopy (NEXAFS). The orbital analysis reveals that the hydrogen bond in melamine is described by the interaction between the triazine nitrogen lone pairs (N_{lp}) and occupied σ(N–H) orbitals, leading to the formation of bonding and antibonding HB states. The antibonding states acquire additional stabilization through a small admixture of the unoccupied σ*(N–H) orbitals of the monomer. Hydrogen bonding is expected to induce splittings of states with lone-pair and σ(N–H) character. In the valence photoemission spectrum, however, these splittings are too small to be resolved directly. In contrast, clear fingerprints of hydrogen bonding emerge in the N 1s NEXAFS spectrum. The MOs derived from the monomer LUMO+1 and LUMO+2, both characterized by σ*(N–H) character, undergo substantial modifications upon hydrogen-bond formation, including orbital mixing, changes in spatial localization, and a redistribution of spectral intensity over a broad photon-energy range. These effects lead to measurable shifts and intensity changes in the NEXAFS resonances, providing direct spectroscopic evidence of the hydrogen-bond-induced perturbation of the electronic structure and supporting the molecular-orbital description of hydrogen bonding in a complex organic supramolecular network.

Received 8th June 2026,
Accepted 9th August 2026

DOI: 10.1039/d6cp02153k

rsc.li/pccp

Introduction

Melamine (M) is one of the smallest organic molecules capable of forming robust hydrogen-bonded architectures, ranging from molecular co-crystals[1–9] to two-dimensional (2D) self-assembled networks on surfaces.[10–18] On suitable substrates, melamine forms ordered porous networks either alone or in combination with a variety of hydrogen-bonding molecules, including cyanuric acid (CA),[19–23] perylene tetracarboxylic diimide (PTCDI),[14,24] perylene tetracarboxylic dianhydride (PTCDA),[25] naphthalene tetracarboxylic diimide (NTCDI),[26,27] or other ditopic imide linkers.[26] Melamine-based 2D assemblies find broad application in supramolecular chemistry, particularly in surface functionalization,[20,22] in catalysis or photocatalysis as precursor for carbon nitride-based catalysts,[19] or as support or buffer layer.[18,21,28]

The H bond (X–H···Y) is the driving force behind self-assembly as it provides a highly directional attractive interaction[19] between the X–H group of one molecule or molecular group with the Y atom of another molecule or molecular group.[29] Typically, the H donor (X) is an electronegative atom, while the H acceptor (Y) is an atom with a region of excess negative charge, *e.g.* an atom with lone pair (lp) electrons.[29] H bonding covers a broad range of phenomena,[30] including some that do not fit the traditional definition.[31,32] Therefore, different criteria to identify, classify, and characterize H bonding

[a] *Faculty of Physics, Astronomy and Informatics, Nicolaus Copernicus University in Torun, Torun, Poland. E-mail: iubr@umk.pl*
[b] *CNR-Istituto Officina dei Materiali, SS 14 km 163.5, 34149 Trieste, Italy*
[c] *Department of Physics, University of Trieste, Via A. Valerio 2, 34127 Trieste, Italy*
[d] *Department of Physics and Astronomy, Uppsala University, P.O. Box 524, 752 20 Uppsala, Sweden*
[e] *CNR-Istituto Struttura della Materia, SS 14 km 163.5, 34149 Trieste, Italy*
[f] *Department of Chemical and Pharmaceutical Sciences, University of Trieste, Via L. Giorgieri 1, Trieste, 34127, Italy. E-mail: valeria.lanzilotto@units.it*
† Current affiliation: School of Chemistry, University of Birmingham, Edgbaston, Birmingham B15 2TT, UK.
‡ Current affiliation: School of Integrated Circuits and Electronics, Beijing Institute of Technology, 100081 Beijing, People's Republic of China.
§ Current affiliation: International Science Programme, Uppsala University, P.O. Box 524, 752 20 Uppsala, Sweden.

have been proposed.[29–31,33,34] Experimentally, H bonding can be identified using different spectroscopies, from rotational spectroscopy in gas phase,[35] to infrared (IR) spectroscopy,[29,30,33,35] nuclear magnetic resonance (NMR),[29,30,33,35] X-ray photoelectron spectroscopy (XPS),[36–40] near-edge X-ray absorption fine structure (NEXAFS),[36,37,39–43] and others.[33]

From a theoretical perspective, there are many approaches to decompose the H bonding interaction energy within different partitioning schemes,[33,44–53] as well as theoretical analysis tools[54–61] such as bond critical points,[60] or natural bond orbitals (NBOs).[5–8,57–60] Furthermore, the H bond can be identified in difference density plots through its characteristic signature of alternating excess and depletion regions, as illustrated for DNA base pairs dimers by Kelly and co-workers.[62–66] However, while providing insights into the nature of the H-bond itself, these approaches lack a direct connection to spectroscopies that directly probe the electronic structure of matter, such as valence level photoemission spectroscopy (VL-PES) or NEXAFS (for the unoccupied energy levels). A molecular orbital (MO) description, on the other hand, naturally links the electronic structure underlying hydrogen bonding to its spectroscopic signatures. In this context, the pioneering work of A. Nilsson and co-workers[41,42,67,68] represents one of the few examples in which electron spectroscopies have been combined with molecular orbital theory to elucidate the electronic structure of liquid water and ice. By comparing isolated molecules with hydrogen-bonded systems, the spectroscopic changes induced by hydrogen bonding could be directly interpreted in terms of molecular orbital interactions. However, beyond this seminal work, a comparable MO/spectroscopy-based framework has not been established for small organic molecules forming hydrogen-bonded assemblies. In particular, the occupied electronic states have remained largely unexplored by valence-level photoemission spectroscopy, while spectroscopic studies have focused almost exclusively on NEXAFS. Even in the latter case, the molecular-orbital interpretation remains only partial. On the one hand, resonance energy shifts are generally well understood in terms of the changes in the core-level binding energy of the atom involved in hydrogen bonding.[37,39,69–72] On the other hand, the quenching of σ* resonances, although frequently observed experimentally, has received considerably less attention and has rarely been interpreted through a detailed molecular orbital analysis of the unoccupied states involved.[37,43,73]

In terms of molecular orbitals, the H-bond is usually described as a bonding and antibonding interaction between the empty σ*(X–H) fragment orbital (FO) and the occupied lone pair FO on Y (Y_{lp}), as illustrated in Fig. 1a.[34,74] Representative examples of this orbital-based description of H-bonding are provided by C. F. Guerra *et al.* in their studies of DNA base pairs.[74,75] However, even in relatively simple H-bonding complexes, the qualitative orbital description of the H-bond is not always straightforward. For instance, when the Y_{lp} is particularly stable or the occupied σ_{X-H} orbital is relatively high in energy, then the Y_{lp} and σ(X–H) can interact, see Fig. 1b.[34,76] This interaction is intrinsically destabilizing, as it involves two filled orbitals and would lead to an increase in the energy of the corresponding (occupied) HB antibonding molecular orbital. This destabilization is mitigated through mixing of the antibonding orbital with higher-energy unoccupied FOs, which lowers its energy. Overall, this leads to a reduction in the total energy of the H-bonded complex. An example of this type of H-bonding description, which is less common, has been proposed for the ClH···NH3 interaction[34] and the hydrogen-bonded water dimer.[76,77]

In this context, the present work aims to investigate the nature of the orbital interactions that best describe the hexagonal supramolecular hydrogen-bonded configuration commonly observed for melamine when adsorbed on Au(111)[11,12,14–16] or Ag(111).[17] Which of the two HB pictures illustrated in Fig. 1 describes a melamine H-bonded network best and how does this theoretical description relate to electronic spectroscopies, such as NEXAFS and VL-PES? To answer these questions, we perform a detailed density functional theory (DFT) analysis of

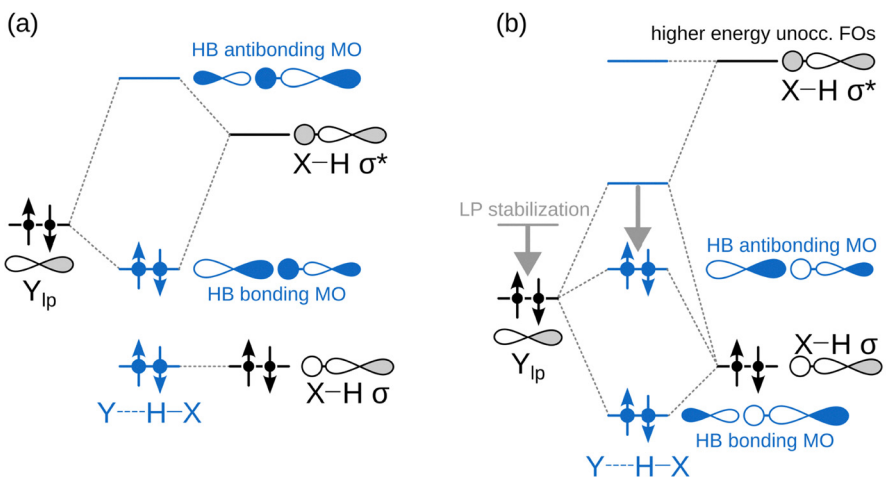

Fig. 1 (a) Formation of a H-bond through the interaction between the Y lone pair orbital with the unoccupied X–H σ* orbital. (b) Formation of a H-bond through the interaction of a stabilized Y lone pair orbital with the occupied X–H σ orbital. In this case, both the bonding and antibonding H-bonding (HB) molecular orbitals (MO) are occupied. Adapted from ref. 34.

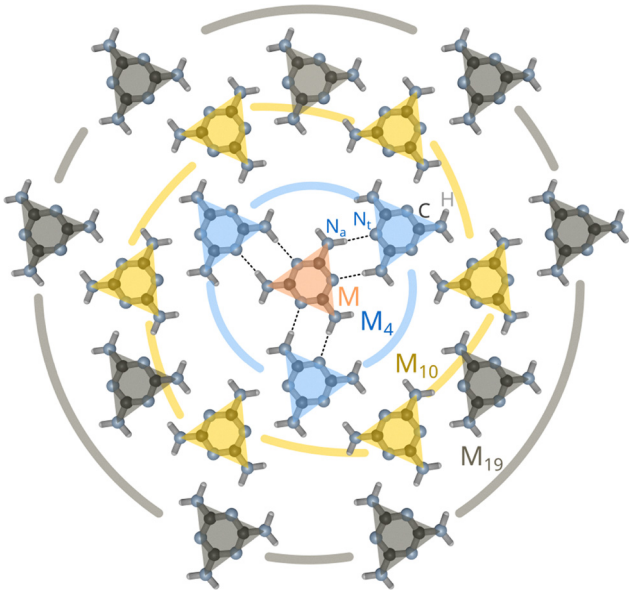

Fig. 2 Molecular structure of melamine in a 2D honeycomb configuration. The dotted lines mark the six H bonds formed by the central melamine molecule with its nearest neighbours. N_a and N_t indicate the amine and triazine N atoms, respectively. The circles of different colors mark the borders of the different models used for the H bonded network: four melamine molecules (M_4), ten melamine molecules (M_{10}), and nineteen melamine molecules (M_{19}).

the in-plane molecular orbitals of the tetramer structure (M_4) shown in Fig. 2, adopted here as a minimal model of the extended network. Within this framework, we elucidate how Y_{lp}, σ*(X–H), σ(X–H) FOs of the individual molecules interact to form the HB antibonding and bonding orbitals that define melamine-based self-assembled structures. Theoretical results are supported by experimental data, including VL-PES and NEXAFS measurements, conducted in both the gas phase (isolated molecule) and on the Au(111)-supported system. In condensed-phase PE spectra, the intrinsic broadening of the valence features hampers the detection of subtle fingerprints associated with H-bonding. By contrast, the interaction is more effectively probed through the investigation of the unoccupied states, particularly *via* NEXAFS measurements at the N K-edge.

Computational details

A hexagonal melamine monolayer was adsorbed and relaxed on the Au(111) surface using density functional theory with the functional by Perdew, Burke, and Ernzerhof (PBE)[78,79] as implemented in the Vienna *ab initio* simulation package (VASP).[80–83] The kinetic energy cutoff for the plane wave basis was 700 eV. The Au(111) surface was modeled using a supercell of 10 × 10 × 3 Au atoms. The lowest Au layer was fixed during structure relaxation and 14 Å of vacuum were added in the *z*-direction to avoid residual interactions between periodic images.[37] Dispersion corrections were included using the D3 model by Grimme and co-workers.[84] PBE-D3 was shown to reliably predict molecular adsorption geometries on Au(111),[85] while the PBE functional is able to describe the geometry of HB systems, especially for linear X–H···Y hydrogen bonds,[86] as is the case for melamine. However, PBE largely underestimates the HOMO–LUMO gap of organic semiconductors, as well as contracts the valence electronic structure.[87,88] Therefore, the valence electronic structure of melamine and corresponding electronic spectra were computed instead with the HSE06 functional which corrects these issues.[89,90] To model the H-bonded melamine monolayer, oligomers of different sizes were cut from the relaxed periodic calculation. We considered the monomer (M), dimer (M_2), tetramer (M_4), decamer (M_{10}), and an oligomer with 19 molecules (M_{19}), as depicted in Fig. 2. Here, the monomer was used as a model for gas-phase melamine, while the larger oligomers were used as models for the H-bonded melamine layer. Removing the Au substrate from our computational models is motivated by a very weak hybridisation between melamine molecules and the Au(111) states, where the physisorbed melamine molecules remain highly mobile on the surface.[16,91] The valence electronic structure for these free-standing oligomers was computed to determine how the oligomer size affects the valence levels in comparison to VL-PES measurements. Among the oligomers, the tetramer is the smallest one which features a fully H-bonded melamine molecule (the central melamine, see Fig. 2), so this model was used to analyze the melamine hydrogen bond in terms of molecular orbitals. Additionally, the changes in the valence electronic structure going from the tetramer to the decamer and to M_{19} are small, see Results and Discussion. Note that throughout the manuscript subscripts are used to label oligomers of different sizes (M_4 – tetramer, M_{10} – decamer, *etc.*), while M_1, M_2, M_3, and M_4 label the individual molecules part of a tetramer.

The valence electronic structure was calculated in Gaussian 16[69] using the HSE06 density functional[70–76] and the 6-31G(d,p) basis set.[77] Additionally, the ground state electronic structures of the monomer, dimer, and tetramer were also computed with using the HSE06 density functional[92–98] and the cc-pVTZ basis set,[99] as implemented in the Psi4 software package.[100] The discrete spectrum of orbital energies (total density of states, TDOS) was broadened using Gaussians of 0.2 eV full width at half maximum (FWHM) to facilitate the comparison to experiment. A further decomposition of the valence peaks into their atomic orbital components was performed using the c^2 method[101,102] to obtain the projected density of states (PDOS). In the case of the dimer and tetramer, the electronic bands were further analyzed as a linear combination of monomer orbitals. For this purpose, the molecular orbital (MO) coefficients of the dimer (tetramer) were represented in the basis of two (four) monomer orbitals calculated separately. In essence, this represents a recasting of the dimer (tetramer) orbitals from the atomic orbital (AO) basis to the basis of monomer molecular orbitals (MMO) achieved by solving a matrix equation for the unknown coefficients of the monomer basis (**X**),

$$\mathrm{MO}_i = \sum_{\mu} c_{\mu i}\mathrm{AO}_{\mu} = \sum_{m}^{M} x_{pi}^{m}\mathrm{MMO}_p^m \qquad (1)$$

where the monomer MOs are determined in the AO basis as,

$$\mathrm{MMO}_p^m = \sum_\nu c_{\nu p}^m \mathrm{AO}_\nu^m \quad (2)$$

Because the oligomer AOs correspond exactly to the AOs from the monomer calculations, eqn (1) and (2) can be combined to obtain a matrix eqn (3) for the unknown monomer basis coefficients,

$$(\mathbf{C}_1 \quad \mathbf{C}_2 \quad \ldots \quad \mathbf{C}_M)\begin{pmatrix} \mathbf{X}^1 \\ \mathbf{X}^2 \\ \vdots \\ \mathbf{X}^M \end{pmatrix} = \mathbf{C} \quad (3)$$

In the equation above, $\mathbf{C}_k$, $k = 1 \ldots M$, are the matrices of MO coefficients for the individual monomers, $\mathbf{C}$ is the matrix of MO coefficients of the oligomer, $\mathbf{X}^k$ are matrices of the unknown monomer orbital coefficients we are after, and M is the total number of monomers. This change of basis allows us to determine the percentage by which each monomer orbital contributes to a given oligomer orbital.

Finally, to determine the effects of H bonding on the unoccupied molecular orbitals, we compute the near-edge X-ray absorption fine structure (NEXAFS) spectra of the monomer, dimer and tetramer. The NEXAFS calculations were performed in psiXAS[103] using transition-potential density functional theory (TP-DFT) with the HSE06 functional.[92–98] Orbital relaxation was modeled using a half core–hole (HCH) localized on the beta 1s orbital of the core-excited atom. Since delocalization of the core hole can introduce errors,[104] the localization of the CH was ensured by replacing the 1s electrons of the non-core-excited N atoms by effective core potentials (ECPs) of the Stuttgart-Cologne type (the ECP2MWB pseudopotential)[105] obtained from the Basis Set Exchange (BSE) database.[106] All electrons of the C atoms and the valence electrons of the non-core-excited N atoms were described using the cc-pVTZ basis set.[99] The aug-cc-pVTZ basis set[107,108] was used for the core-excited N atom and the cc-pVDZ basis set[99] was used for H. A separate NEXAFS spectrum was computed for each N atom in the monomer, as well as for each N atom of the central melamine molecule in the tetramer, in order to model a H-bonded melamine in a monolayer. The discrete spectra were broadened using Gaussian functions with a constant FWHM of 0.4 eV and shifted by 0.42 eV to lower photon energies in order to align the monomer π* peak to the experimentally measured π* peak in the gas-phase. A total spectrum was calculated by summing the individual N atom spectra together. The volumetric data of ground state orbitals and orbitals relaxed in the presence of a half-core–hole was determined using ORBKIT 1.1.0,[109] then visualized using Jmol[110,111] and Blender 3.6.[112]

Experimental methods

Melamine was purchased from Sigma Aldrich (purity 99%) and sublimed in a temperature range between 390–403 K. Gas phase measurements were performed at the GasPhase beamline of the Elettra Synchrotron (Trieste, Italy), using a Scienta SES-200 hemispherical analyzer. VL-PE spectra were acquired with a photon energy of 40 eV and an energy resolution of 50 meV. The calibration of the ionization energy scale was made through the simultaneous acquisition of the Ar 3p line ($P_{\mathrm{Ar}} = 2.4 \times 10^{-6}$ mbar) and aligning the Ar $3p_{3/2}$ component to 15.76 eV.[113] For details on the NEXAFS measurements of gaseous melamine, we refer the reader to our previous publication.[37] Solid state photoemission measurements were performed at the "Surface Physics" Laboratory of Uppsala University, using a Scienta SES-100 hemispherical analyzer coupled with a helium-light source (Scienta Omicrom VUV5000). A thick film of melamine was deposited on a Au(111) surface, after sputtering and annealing cycles. The VL spectrum was acquired with $h\nu$ = 40.8 eV (HeII) and a final energy resolution of 200 meV (Fermi edge FWHM). The calibration of the binding energy scale was made by measuring, just before the deposition, the Fermi level of the clean Au(111) substrate. Details on the NEXAFS measurements of the melamine monolayer/Au(111) (1.2 ML) are provided in ref. 39.

Results and discussion

Hydrogen bonding effects on the occupied valence levels

Fig. 2 displays a representative portion of the hexagonal supramolecular network typically formed by one monolayer of melamine molecules adsorbed on Au(111).[11,12,14–16] As indicated by the dotted lines, each melamine unit simultaneously acts as a hydrogen donor *via* its amino nitrogen (N_a) and as a hydrogen acceptor *via* the triazine nitrogen (N_t), forming a total of six hydrogen bonds.

The lower part of the graph shown in Fig. 3a presents the total density of states (TDOS) calculated for an isolated, non-interacting melamine molecule (M, filled yellow curve), along with the projected density of states (PDOS) on the π (blue curve) and σ (red curve) orbitals localized on the nitrogen atoms. The upper part of the graph shows the corresponding TDOS and PDOS for unsupported hydrogen-bonded assemblies having increasing numbers of melamine units—specifically, four (M_4), ten (M_{10}), and nineteen (M_{19}) molecules—as indicated by the colored circles in Fig. 2. The TDOS of the monomer is compared with the valence-level PE spectrum of gas phase (GP) melamine (dotted black line). The bottom axis reports the experimental ionization energy scale and the theoretical curves were shifted to align the first peak (HOMO*, the asterisk marks degenerate states, see below) with band A. In contrast, the TDOS of the hydrogen-bonded structures (M_4, M_{10}, M_{19}) are compared with the valence PE spectrum acquired from a thick film (TF) of melamine adsorbed on the Au(111) surface. The binding energy scale of the solid state spectrum is reported on the top axis and the theoretical curves were shifted to align the "ab" band with the first group of bands comprising HOMO*-like, H−2-like and H−1*-like MOs. Multilayer spectra are generally preferred over monolayer spectra, as the latter tend

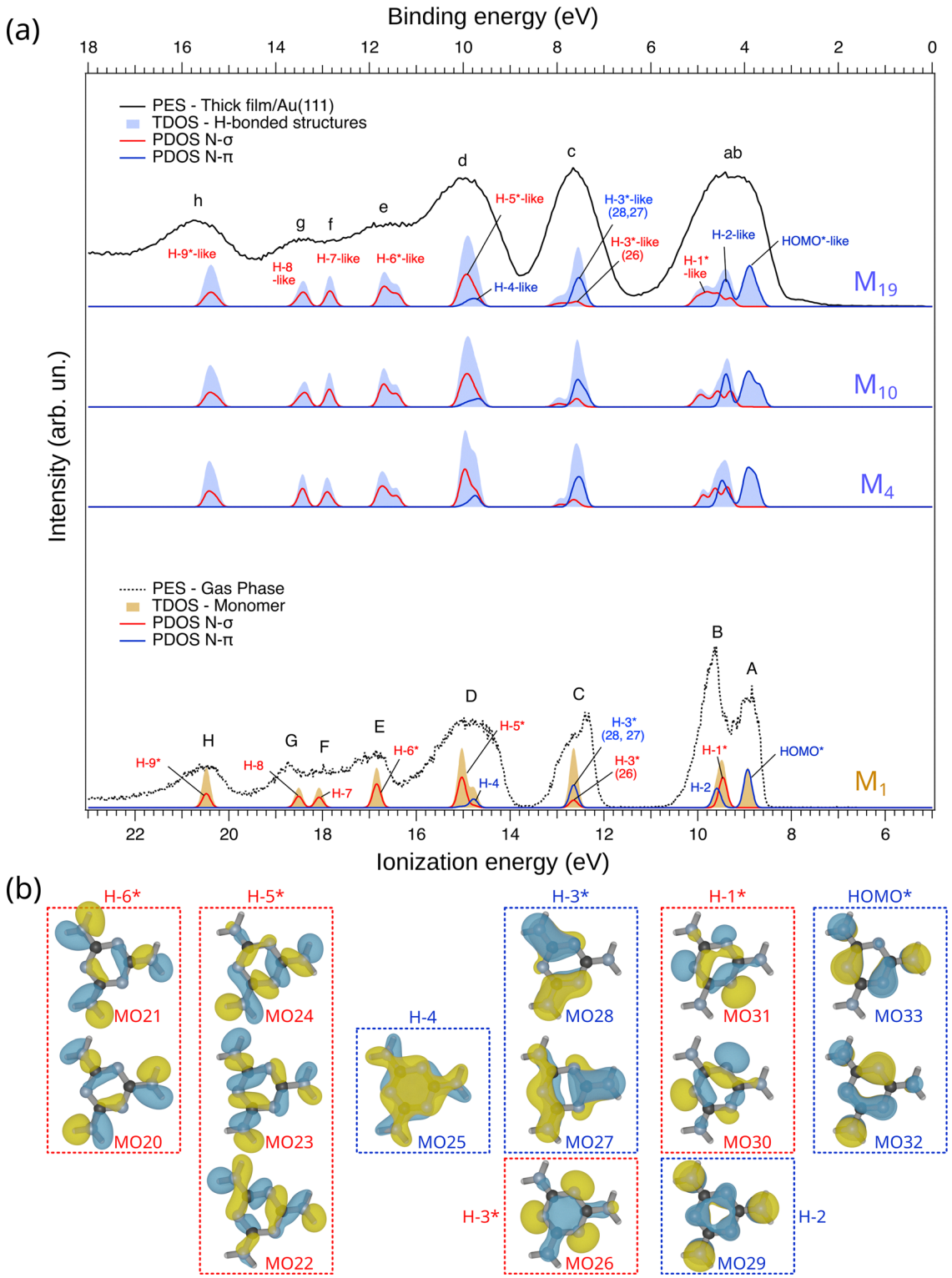

Fig. 3 (a) Comparison between the experimental valence PE spectrum of gaseous melamine and the TDOS computed for the isolated melamine (graph denoted with M), alongside valence PES results of melamine adsorbed as thick film on Au(111) and the comparison with the TDOS computed for several H-bonded structures (curves M_2–M_{19}). For each structure, PDOS projected on the σ and π states on N are also reported. The occupied DOS are plotted on a positive energy scale and shifted to match the binding energy position of the corresponding first spectral feature (band A or band ab). (b) Top view of the molecular orbitals of the melamine monomer represented using a wave-function isosurface absolute value of 0.035 a.u. Positive isosurfaces are shown in blue, while negative isosurfaces are shown in yellow.

to be less informative due to the dominant contribution of substrate features. Nonetheless, previous studies showed that the planar arrangement of the monolayer is preserved in the upper layers of thicker films, suggesting that the hexagonal

hydrogen-bonded network is likewise maintained.[37,40] Indeed, both the N 1s XPS and NEXAFS spectra of these multilayer systems closely resemble those of the monolayer phase (with some broadening of the spectral features) and are both reasonably well reproduced using unsupported hydrogen-bonded models based on the M_4 configuration.[37]

The valence PE spectrum of gaseous melamine is characterized by eight features (labeled from A to H), which are well reproduced by the monomer (M) simulation. Band A at about 8.9 eV derives from the HOMO* level, a double degenerate state with π character (degenerate states are marked with an asterisk *, *i.e.* HOMO*). Band **B** stands for the HOMO−1* and the HOMO−2. The latter is a π-orbital, while the HOMO−1* is a σ-orbital with a strong lone-pair character deriving from the triazine N atoms (N_{lp} FOs). Band **C** arises from the HOMO−3*, a three-degenerate state that comprises two states with pure π character (MO28, MO27) and one state of σ character (MO26), the latter featuring N_{lp} FOs. Band D, instead, is contributed by the HOMO−4, a π-orbital, and a three-degenerate state with σ-character (HOMO−5*) with electron charge density localized on the N–H termini, that is σ(N–H) FOs. Similar σ-orbitals (HOMO−6*) also contribute to band E. The above-mentioned molecular orbitals are shown in Fig. 3(b).

As for the H-bonded clusters, the number of MOs increases by a factor of 4 (M_4), 10 (M_{10}) and 19 (M_{19}). These oligomers were considered to assess the effect of the network size on the electronic structure. As will be shown later, the charge distributions associated with the MOs in the H-bonded structures strongly recall those of specific monomer orbitals, but with a different weighting for each molecule. Therefore, the new orbitals will be grouped according to the similarity with the parental ones and named as (HOMO*)-like MOs, (H−1)*-like MOs and so on (see the labeling in Fig. 3a). Each group of MOs forms a well-defined band, leading to a TDOS that reflects the underlying monomer-derived orbital character. As the oligomer size increases, these bands become progressively broader, especially those with σ character, while their overall energy distribution and orbital character remain essentially unchanged. This progressive broadening likely explains the appearance of a single "ab" band in the film (top panel of Fig. 3a), rather than the two well-resolved peaks observed for the gas phase (bands A and B, bottom panel of Fig. 3a). Despite the overall agreement between experiment and theory, the spectroscopic effects of hydrogen bonding on the occupied valence states are too subtle to be unambiguously resolved in the measured photoelectron spectra. A detailed analysis of the occupied states is nonetheless essential to clarify how the monomer orbitals mix upon H-bonded formation, and in particular to distinguish between the interaction schemes proposed in Fig. 1. In the following, we therefore proceed with an in-depth analysis of the occupied levels, while anticipating that a much stronger experimental validation of the calculations will be provided by the analysis of the unoccupied states.

Since H-bonding interactions involve σ-orbitals and occur within the molecular plane, we restrict our analysis to σ-type MOs and do not consider orbitals with π character. Moreover, given the large number of orbitals involved, the discussion is limited to the tetramer (M_4), which represents the smallest unit in which at least one melamine molecule is fully engaged in H-bonding interactions. As larger oligomers mainly produce additional spectral broadening without qualitatively modifying the orbital interactions, the tetramer is sufficient to capture the essential electronic effects of hydrogen bonding.

Fig. 4 shows the orbital interaction diagram of the tetramer, with the energy scale reported on the left axis. The horizontal bars on the left and right of the diagram correspond to the energy levels of the central melamine (M_1) and of the peripheral molecules (M_2, M_3, M_4), respectively. Tetramer levels are displayed in the center. Blue and red bars denote MOs with predominant π and σ character, respectively. Violet bars identify MOs with mixed π/σ character (see those deriving from the

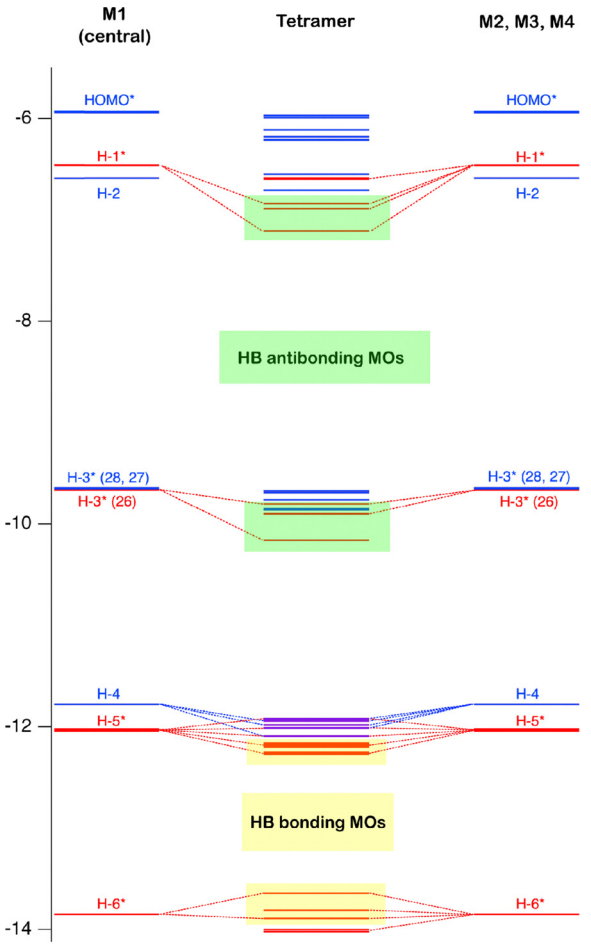

Fig. 4 Orbital interaction diagram of the tetramer. Central bars represent the molecular orbitals (MOs) of the tetramer, while left and right bars indicate the MOs of the central (M_1) and peripheral molecules (M_2, M_3, M_4, respectively). Red and blue bars indicate orbitals with σ and π character, respectively, while violet bars represent MOs with mixed σ/π character. Red and violet tetramer levels are connected to those of the central or peripheral molecules when the contribution of at least one monomer orbital is equal to or greater than 10%. Green boxes highlight the σ-type MOs of the tetramer with strong lone pair character and corresponding to HB antibonding MOs, while HB bonding MOs are marked by yellow boxes and can be identified within orbitals with σ(N–H) character.

mixing of H−4 and H−5*). Tetramer levels with mostly or partially σ character are connected to those of the central and peripheral molecules by dashed lines when at least one monomer orbital contribution is ≥10%. The detailed quantitative orbital compositions of each tetramer MO are reported in Tables S1–S5. Green boxes highlight the σ-type orbitals with strong "lone-pair" character, which receive some contributions from unoccupied monomer orbitals and which we will see correspond to the HB antibonding orbitals. In yellow, on the other hand, we have highlighted those orbitals with significant contributions from orbitals with σ(N–H) character, where it is possible to identify the HB bonding orbitals. As we will see, this places H-bonding in melamine under the less common HB model depicted in Fig. 1b.

HB antibonding orbitals. Among the HB orbitals, those derived from H−1* and H−3* (MO26), which bear N_{lp} FOs, can be identified as the relevant antibonding combinations. Since the H−1*- and H−3*-like orbitals provide essentially the same physical picture, we focus here on the H−3*-like MOs, while the corresponding H−1*-like orbitals are discussed in the SI (Fig. S2). The energy diagram of the H−3*-like MOs is shown in the left panel of Fig. 5. The diagram is built with the same features described for the diagram of Fig. 4. The tetramer levels of σ-character are connected to those of the central and peripheral molecules by red dashed lines when at least one monomer orbital contribution is ≥10%. Additional gray dashed lines are reported when the orbital participation is lower than 10% but ≥0.1%. For clarity, contributions from MOs that lie far above and below the H−3* energy levels are grouped together and arbitrarily positioned along the energy scale. The exact orbital contributions can be found in the SI, Table S2.

The orbital representations shown alongside the energy diagram in Fig. 5 correspond to the H−3*-derived MOs of the tetramer (MO107, MO103, MO102, and MO101), all contributing to the hydrogen-bonding interactions. In MO101, the central molecule mainly contributes through the H−3* (52.03%) whereas the external molecules provide only minor H−3* contributions. Interestingly, the latter also show additional faint charge densities along the hydrogen-bonded N–H termini (see dashed circles), which cannot be assigned to H−3*. These features originate from the mixing with several occupied MOs containing σ(N–H) FOs, mainly H−5* (*ca.* 1.3%) and H−6* (*ca.* 0.7%). Conversely, in MO102 and MO103, the external molecules show significant H−3* contributions, whereas the central molecule only show amino charge densities mainly deriving from H−5* and H−6*. Finally, MO107 receives nearly equal H−3* contributions from all molecules and displays additional charge densities at the hydrogen-bonding N–H termini, mainly arising from the H−5* and H−6*. Notably,

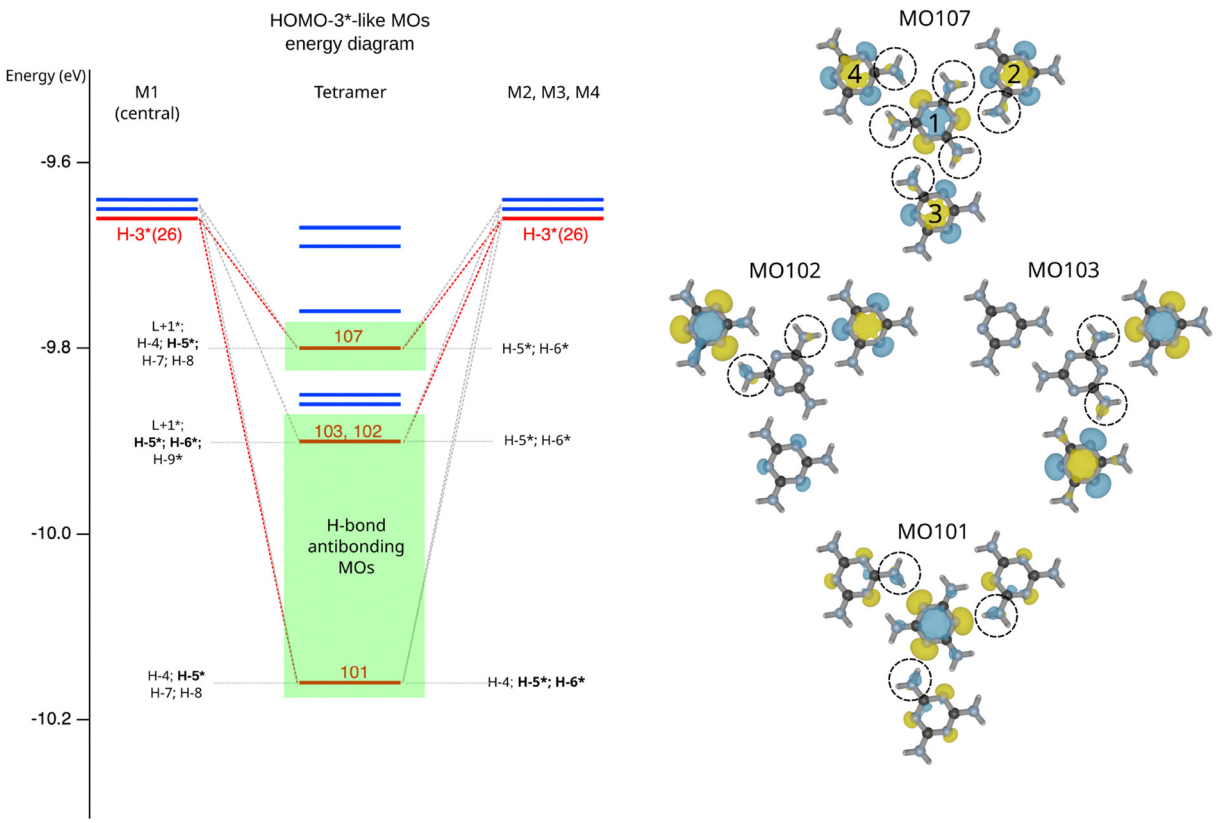

Fig. 5 Molecular orbital diagram and molecular orbitals of the melamine tetramer, focussing on the (HOMO−3)*-like HB anti-bonding orbitals: MO101, MO102, MO103, and MO107. Positive isosurfaces are shown in blue, while negative isosurfaces are shown in yellow, represented using 0.035 a.u. for the wave-function isosurface absolute value.

MO102, MO103, and MO107 also exhibit small contributions from the unoccupied L+1* orbital, which contains σ*(N–H) FOs.

Overall, these MOs arise primarily from the mixing of N_{lp} FOs with occupied σ(N–H) FOs, with only minor contributions from unoccupied σ*(N–H) FOs. A common characteristic of this manifold is the out-of-phase coupling between the facing lone-pair and σ(N–H)/σ*(N–H) charge densities, identifying these orbitals as the H-bond antibonding MOs.

Interestingly, MO101 and MO107 differ in the relative phase of the N_{lp} FOs on adjacent molecules. While the corresponding fragments are in-phase in MO101, they are out-of-phase in MO107. This phase difference results in an energy splitting of approximately 0.3 eV between the two MO pairs, with the in-phase MO101-derived pair lying at lower energy.

HB bonding orbitals. We now focus on the innermost σ-type orbitals, specifically those featuring significant contribution from HOMO−5* and HOMO−6* MOs (for an overview see Fig. 4). As a representative example, we discuss the H−6*-derived MOs, shown in Fig. 6. The detailed monomer contributions are given in Table S5. HOMO−5*-like orbitals are reported in the SI (Fig. S3–S5), together with their analysis. We briefly note that the high energy H−5*-derived MOs (marked in purple in Fig. 4) mix with π orbitals derived from parental H−4. Despite the mixed-symmetry character, contributions from H−1* or H−3* FOs clearly indicate their involvement in H-bonding (see Table S3 and Fig. S5).

HOMO−6*-like orbitals are shown in Fig. 6 along with the corresponding energy diagram. All MOs display pronounced H−6* contributions on central and/or peripheral molecules. To a lesser extent, some molecules also contribute *via* the H−3* and H−1*; such contributions (lone pair-like features) can be readily identified in the central molecule of MO82 and in the peripheral ones of MO81 and MO80 (see dashed circles). Notably, none of the H−6*-like orbitals contain contributions from the unoccupied MOs with σ*(N–H) FOs (see Table S4). Facing N_{lp} and σ(N–H) FOs are in-phase, confirming the bonding nature of these H-bond orbitals. Moreover, MO84/MO83 and MO81/MO80 show, respectively, an anti-phase and in-phase coupling between the σ(N–H) FOs of the peripheral molecules and that of the central one with an energy splitting of 0.25 eV.

In summary, we have identified for the melamine tetramer a set of HB antibonding orbitals (H−1* and H−3*-like) and HB bonding orbitals (H−5* and H−6*-like). The HB antibonding orbitals arise from the mixing of N_{lp} FOs (H−1*, H−3*(26)) with occupied σ(N–H) FOs (H−5* or H−6*), including a very small stabilizing contribution from the unoccupied σ*(N–H) FOs. As discussed in the main text for the H−3*-like orbitals, this contribution mainly originates from L+1*, while the analogous

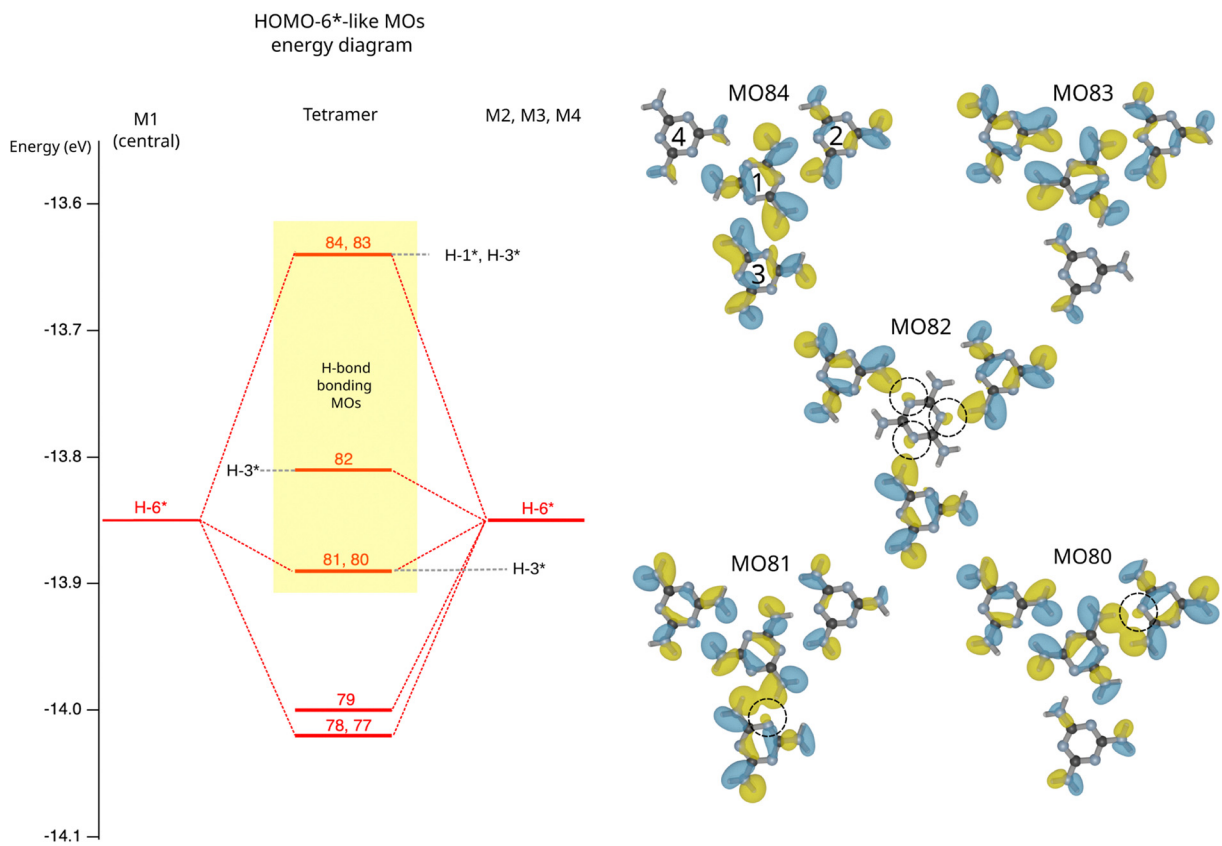

Fig. 6 Molecular orbitals diagram of the melamine tetramer, with a focus on the HOMO-6*-like HB bonding orbitals: MO84-MO77. Positive isosurfaces are shown in blue, while negative isosurfaces are shown in yellow, represented using 0.035 a.u. for the wave-function isosurface absolute value.

H−1*-like orbitals also involve L+2* (see discussion in the SI). The HB bonding orbitals feature only interactions between the N_{lp} and σ(N–H) FOs. These features are consistent with the model presented in Fig. 1b, where the interaction between two occupied orbitals, N_{lp} and σ(N–H), generates an HB antibonding MO relatively high in energy which is subsequently stabilized through mixing with higher-energy unoccupied MOs with σ*(N–H) character, such as L+1* and L+2*. The formation of HB bonding and antibonding orbitals results in a splitting of the energy levels which would result in a broadening of the VL-PES bands, however the energy separation among the orbitals belonging to the same group (*e.g.*, H−3*, H−6*) is only a few tenths of an electronvolt (0.3/0.25 eV), making it practically undetectable by VL-PES. In contrast, hydrogen-bonding effects are more pronounced in NEXAFS spectra, as previously testified for liquid water/ice.[41,42]

Hydrogen bonding effects on the unoccupied valence levels

Fig. 7(a) compares the measured gas-phase N 1s NEXAFS spectrum of melamine with the spectrum calculated using

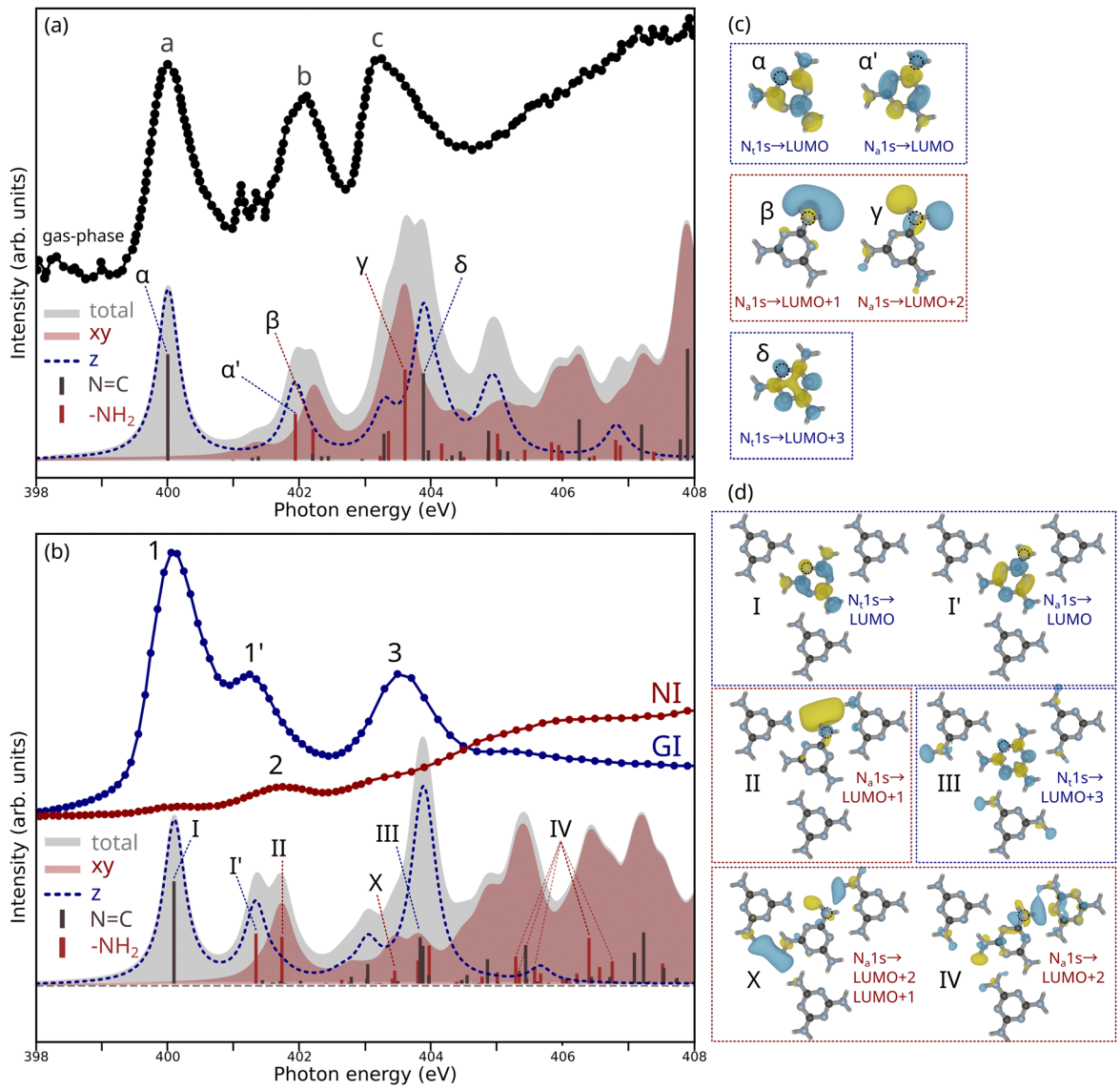

Fig. 7 (a) The NEXAFS spectrum of gas-phase melamine from ref. 37 compared to the computed NEXAFS spectrum for a melamine monomer using TP-DFT with the HSE06 density functional. (b) NEXAFS spectrum of a 1.2 monolayer of melamine deposited on Au(111) from ref. 39 compared to the computed spectrum of the central melamine of the tetramer. The calculated monomer spectrum was shifted by −0.42 eV to align its first peak with experimental resonance a, while the tetramer was shifted by −0.59 eV to align its first peak with experimental peak 1. The total calculated spectra are decomposed into in-plane (*xy*, filled red curve) and out-of-plane (*z*, blue dotted line) components. The bar graphs corresponding to triazine (N = C, N_t) N 1s transitions are shown in brown, while those corresponding to amine (–NH_2, N_a) N 1s transitions are shown in orange. (c) and (d) Excited unoccupied MOs in presence of a HCH on the amino or triazine N 1s orbital for the (c) monomer and (d) tetramer, respectively. The atom with the HCH is indicated by a black circle. Positive isosurfaces are shown in blue, while negative isosurfaces are shown in yellow, represented using a wave-function isosurface absolute value of 0.035 a.u.

TP-DFT with the HSE06 density functional (shown in gray) for a melamine monomer. The theoretical spectrum is further decomposed into in-plane and out-of-plane contributions, with individual resonances highlighted by brown sticks for those involving the N_t, and red sticks for those associated with the N_a.

The experimental spectrum has three main features denoted a, b, and c, which are reproduced remarkably well by the calculation allowing us to assign the experimental peaks. Feature a originates solely in the transition from the 1s of the N_t to the doubly degenerate LUMO of π* character (resonance α), depicted in Fig. 7(c). Peak b has both π* and σ* contributions as it is composed of two separate features, one originating from the transition of the N_a 1s electron to the LUMO (resonance α′), and the other from the transition of the N_a 1s electron to LUMO+1 (resonance β), a triply degenerate orbital featuring σ*(N–H) character. In the presence of the HCH, this orbital localizes over the $–NH_2$ termination where the core–hole is located, see Fig. 7(c). The energy separation between the α and α′ resonances (*ca.* 1.9 eV) is essentially determined by the difference in the ionization energies (IEs) between N_t and N_a (see Fig. S6).[37]

Feature c has several different contributions of both π* and σ* character, but the two main ones with the largest intensity arise from the transition of the N_a 1s electron to LUMO+2 (resonance γ), a triply degenerate orbital of σ*(N–H) character, and from the transition of the triazine N 1s electron to LUMO+3 of π* character (resonance δ). As shown, resonances β and γ involve transitions to σ* orbitals polarized toward the hydrogen atoms and are therefore expected to be the most sensitive to hydrogen bonding, as indeed observed.[37,42]

Fig. 7(b) shows the computed in-plane and out-of-plane NEXAFS spectra of the tetramer's central molecule, a representative model of a fully H-bonded melamine molecule in the film, compared with experimental data for 1.2 ML of melamine on Au(111).[39] Solid-state measurements were performed with two different scattering geometries, at normal incidence (NI, electric field vector **E** parallel to the surface plane) and grazing incidence (GI, electric field vector **E** almost perpendicular to the surface plane). As melamine is adsorbed flat enhancement of π* and σ* resonances occur at GI and NI, respectively. As in the monomer case, the agreement between theory and experiment is excellent.

Resonances I and I′ correspond to excitations from the triazine and amino N 1s levels, respectively, into a LUMO-derived state localized on the central molecule, closely resembling the α and α′ resonances of the isolated molecule. Compared to the monomer, the energy separation between these two resonances is reduced by 0.67 eV, consistent with a lowering of the ionization energy (IE) of the N_a 1s level when going from the isolated to the H-bonded phase (see Fig. S4 and ref. 37). Resonance I and resonance I′ clearly correspond to peak 1 and 1′ of the experimental spectrum taken in GI, confirming their out-of-plane nature.

Another characteristic feature of the tetramer, like that observed in the isolated molecule, is the pronounced π* contribution around 404 eV, which can be clearly assigned to peak 3 in the experimental spectrum (GI). One of the transitions associated with this feature originates from the triazine N 1s level and involves a MO mainly derived from the LUMO+3 of the central molecule (resonance III), making it the counterpart of the δ resonance in the isolated molecule.

Having established the relatively minor effects on the π resonances, we now focus on the σ states, which show a much stronger response to hydrogen bonding and thus provide a more sensitive fingerprint of the interaction. Resonance II originates from the amino nitrogen and involves a σ*-type MO which can be identified as the LUMO+1, mainly localized on the central molecule. Relative to its monomer counterpart (resonance β), this state is appreciably modified, showing localization on the uncoordinated N–H bond (Fig. 7c). Further support for this assignment is provided by the NEXAFS analysis calculated for the dimer (see Fig. 8), where transitions from amino N engaged and not engaged in hydrogen bonding can be clearly distinguished. The non-H-bonded N_a gives rise to a transition involving a MO essentially identical to the LUMO+1 (resonance ii′), whereas the H-bonded N_a exhibits a modified LUMO+1 (resonance ii), characterized by the same localization on the uncoordinated N–H moiety as observed for the central molecule in the tetramer. Compared to resonance ii′, resonance ii is shifted to lower photon energy due to the lowering of the IE of the H-bonded N_a. Similarly, resonance II (tetramer) is also shifted to lower photon energy relative to resonance β and reasonably corresponds to peak 2 in the experimental NEXAFS measured in NI. In our calculations, the intensity of this resonance is overestimated with respect to the experiment. In contrast, other computational approaches correctly reproduce its quenched character.[39]

An unambiguous quenching of the σ* intensity is observed around 404 eV, accompanied by a corresponding increase at higher photon energies (compare the red filled curves of the monomer and the central molecule in the tetramer). To further clarify this behavior, it is instructive to compare these results with those obtained for the dimer (see Fig. 8). In the dimer, the non-H-bonded N_a gives rise to resonance iv′, which involves a MO resembling the LUMO+2 of the isolated molecule (resonance γ). At higher energies, at about 406.5 eV, we found resonance iv involving the H-bonded N_a and a MO clearly contributed by LUMO+2. However, the orbital portion localized on the coordinated N–H bond exhibits an unusual orientation, being directed away from the hydrogen-bond axis. Other weaker resonances, labelled $X_{1–3}$, involve MOs with mixed LUMO+2/LUMO+1 character and appear at slightly higher energies than resonance iv′. An example of these $X_{1–3}$ resonances is shown in Fig. 8(b): the LUMO+1 component remains largely unaffected, as it is localized on the part of the molecule not involved in hydrogen bonding, whereas the LUMO+2 component is somewhat distorted and does not exhibit localization on the coordinated N–H group.

In the tetramer's central molecule, the resonance associated with the non–H-bonded N_a is obviously absent, which accounts for the pronounced intensity decrease in this energy region. Resonances involving the LUMO+2 and the H-bonded N_a are

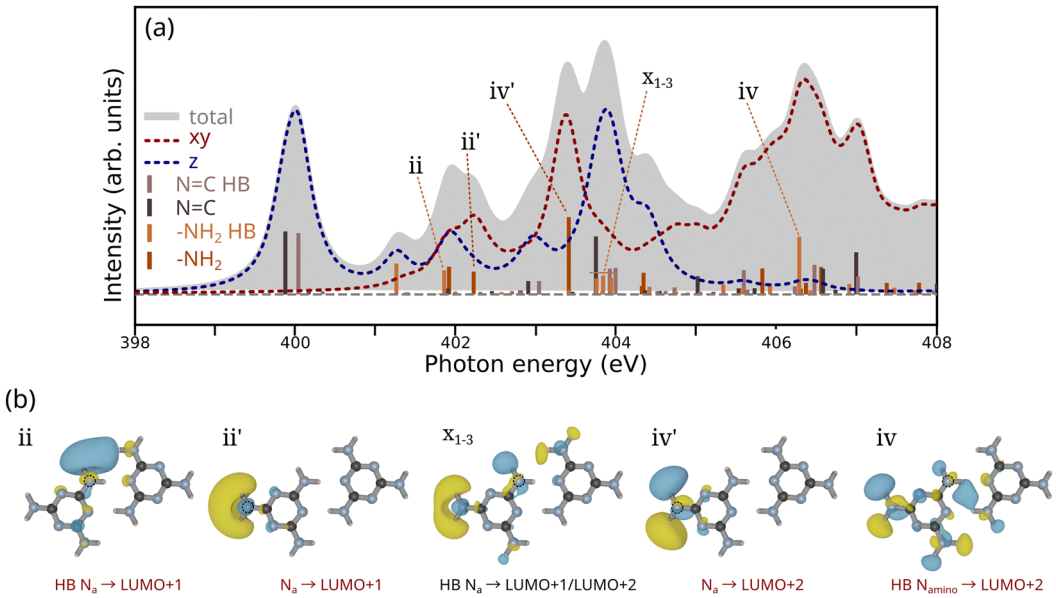

Fig. 8 (a) The calculated NEXAFS spectrum of the melamine dimer shifted by 0.59 eV towards lower photon energies (same as the calculated tetramer). The total calculated spectrum is decomposed into in-plane (*xy*, red line) and out-of-plane (*z*, blue line) components. The bar graphs corresponding to triazine (N = C, N_t) N 1s transitions are shown in brown, while those corresponding to amine ($-NH_2$, N_a) N 1s transitions are shown in orange. H-bonded N atoms are denoted by HB. (b) Excited unoccupied MOs in presence of a HCH on the amino or triazine N 1s orbital. The atom with the HCH is indicated by a black circle. Positive isosurfaces are shown in blue, while negative isosurfaces are shown in yellow, represented using a wave-function isosurface absolute value of 0.035 a.u.

instead distributed at higher photon energies, as highlighted by the dashed lines marked with IV. An example of these transitions is shown in Fig. 7(d), where part of the orbital remains localized on the coordinated N–H group, although not along the H-bond direction, similarly to resonance iv in the dimer. An additional transition, analogous to the X_{1-3} resonances of the dimer and characterized by mixed LUMO+1/LUMO+2 character, is found at lower photon energies and is marked with X in Fig. 7(b). In this case, both the LUMO+1 and LUMO+2 contributions exhibit distorted orientations, mainly localized on the uncoordinated N–H bonds.

Overall, the σ resonances are found to involve LUMO+1- and LUMO+2-derived states whose spatial character is appreciably modified by hydrogen bonding. They exhibit, indeed, a redistribution of orbital density, leading to polarization around either coordinated or uncoordinated N–H groups, generally without alignment along the hydrogen-bond direction. These polarization effects can, to some extent, also be related to the fact that a small fraction of LUMO+1/LUMO+2 contribute to the occupied valence states (HB antibonding MOs). Consistently, these occupied states (H−1*–H−3*-like MOs) exhibit new density localization along the coordinated N–H bonds involved in hydrogen bonding. Finally, the LUMO+1- and LUMO+2-derived excited states are distributed over a wide photon-energy range, which naturally accounts for the reduced intensity (quenching) observed around 404 eV and the corresponding increase at higher photon energies. Similar observations have been made for the O 1s NEXAFS spectra of liquid water and ice compared to gaseous water.[42] Calculations of water dimers have shown that the spectrum of the H donor is largely modified compared to the monomer spectrum. Specifically, the transition from the O 1s to the $2b_2$ MO of water appears to be completely quenched because this peak splits into two new features. One contribution, related to $2b_2$-like dimer orbitals localized on the uncoordinated OH, moves to lower photon energy and mixes with the $4a_1$ feature. The other contribution related to $2b_2$-like orbitals localized on the coordinated OH (but not oriented along the H-bond), moves to higher photon energy.[42] In melamine, we similarly observe both a mixing between LUMO+2 and LUMO+1, as well as a shift to higher energies of the LUMO+2-like orbitals.

Conclusions

In conclusion, this work establishes a molecular-orbital framework to describe hydrogen bonding in extended melamine networks and directly connects the nature of the orbital interaction to its spectroscopic fingerprints. The analysis demonstrates that the hydrogen bond in melamine cannot be fully described by the conventional donor–acceptor picture based on the interaction between a nitrogen lone pair and an empty σ*(N–H) orbital. Instead, the interaction is dominated by the mixing of triazine N lone-pair orbitals with occupied σ(N–H) orbitals, leading to the formation of hydrogen-bonding molecular orbitals with both bonding and antibonding character. The latter acquire a small but significant contribution from higher-energy σ*(N–H)-type orbitals.

This orbital mixing has a direct impact on the electronic structure: in the occupied manifold, it produces a redistribution

and splitting of σ-derived states, experimentally manifested mainly as a progressive broadening of valence photoemission features. Although these effects are subtle, they reveal how hydrogen bonding modifies the occupied electronic levels, a regime that has received considerably less attention compared to unoccupied-state spectroscopies. Conversely, the N 1s NEXAFS spectra provide more pronounced fingerprints of hydrogen bonding, through energy shifts and intensity modulations of the σ*(N–H)-derived resonances, offering a direct experimental probe of the orbital interactions involved. Overall, this work extends the orbital description of hydrogen bonding beyond simple molecular systems and demonstrates how the combination of electron spectroscopies and molecular-orbital analysis can unravel the orbital interactions underlying hydrogen bonding in complex organic networks.

Conflicts of interest

There are no conflicts to declare.

Data availability

Data for this article are available in the RepOD (Repository for Open Data) repository at https://doi.org/10.18150/UVHAXW.

Supplementary information (SI) is available. See DOI: https://doi.org/10.1039/d6cp02153k.

Acknowledgements

We acknowledge the Carl Tygger Foundation, Sweden, for financial support and for making available the VG-Scienta SES-200 photoelectron analyzer at the Gas Phase beamline, Elettra, Italy. VL, CS and MDS also acknowledge the financial contribution provided by the European Union – NextGenerationEU through the Italian MUR PRIN 2022 project ''ODYSSEY'' (2022AXN9EK). The computation was carried out on the Argon and Prime clusters at the Nicolaus Copernicus University in Torun.

References

1 J. A. Zerkowski, J. C. MacDonald, C. T. Seto, D. A. Wierda and G. M. Whitesides, Design of Organic Structures in the Solid State: Molecular Tapes Based on the Network of Hydrogen Bonds Present in the Cyanuric Acid-Melamine Complex, *J. Am. Chem. Soc.*, 1994, **116**, 2382–2391.

2 L. Vella-Zarb, D. Braga, A. G. Orpen and U. Baisch, The influence of hydrogen bonding on the planar arrangement of melamine in crystal structures of its solvates, cocrystals and salts, *CrystEngComm*, 2014, **16**, 8147–8159.

3 T. J. Prior, J. A. Armstrong, D. M. Benoit and K. L. Marshall, The structure of the melamine–cyanuric acid co-crystal, *CrystEngComm*, 2013, **15**, 5838–5843.

4 N. Kanagathara, M. K. Marchewka, M. Drozd, N. G. Renganathan, S. Gunasekaran and G. Anbalagan, Preparation, crystal structure, vibrational spectral and density functional studies of bis(4-nitrophenol)-2,4,6-triamino-1,3,5-triazine monohydrate, *J. Mol. Struct.*, 2013, **1049**, 345–354.

5 S. A. Kalyan, N. Kanagathara, M. K. Marchewka, J. Janczak and K. Senthilkumar, Structure, Spectroscopy, and Theoretical insights on Co-crystals of 2,4-Diamino-6-Methyl-1,3,5-Triazine Bis(4-Aminobenzoic acid) Monohydrate as a promising anti-cancer agent, *Phys. B*, 2024, **679**, 415807.

6 S. A. Kalyan, S. Elangovan, R. Karthick, N. Kanagathara, M. K. Marchewka and J. Janczak, Synthesis, XRD, spectral, photoluminescence, optical, electrical conductivity, and dielectric studies on melamine – melaminium 2-acetyl benzoate dihydrate, *J. Mater. Sci.: Mater. Electron.*, 2024, **35**, 2100.

7 V. Sangeetha, M. Govindarajan, N. Kanagathara, M. K. Marchewka, M. Drozd and G. Anbalagan, Vibrational, DFT, and thermal analysis of 2,4,6-triamino-1,3,5-triazin-1-ium 3-(prop-2-enoyloxy) propanoate acrylic acid monosolvate monohydrate, *J. Mol. Struct.*, 2013, **1054**, 307–320.

8 V. Sangeetha, M. Govindarajan, N. Kanagathara, M. K. Marchewka, S. Gunasekaran and G. Anbalagan, Structure and vibrational spectra of melaminium bis(trifluoroacetate) trihydrate: FT-IR, FT-Raman and quantum chemical calculations, *Spectrochim. Acta, Part A*, 2014, **125**, 252–263.

9 V. Sangeetha, K. Gayathri, P. Krishnan, N. Sivakumar, N. Kanagathara and G. Anbalagan, Growth, structural, crystallisation, thermal decomposition and dielectric behaviour of melaminium bis(hydrogen oxalate) single crystal, *J. Therm. Anal. Calorim.*, 2014, **117**, 307–318.

10 S. Uemura, M. Aono, K. Sakata, T. Komatsu and M. Kunitake, Thermodynamic control of 2D bicomponent porous networks of melamine and melem: diverse Hydrogen-bonded networks, *J. Phys. Chem. C*, 2013, **117**, 24815–24821.

11 S. Uemura, M. Aono, T. Komatsu and M. Kunitake, Two-dimensional self-assembled structures of melamine and melem at the aqueous solution-Au(111) interface, *Langmuir*, 2011, **27**, 1336–1340.

12 H.-M. Zhang, Z.-X. Xie, L.-S. Long, H.-P. Zhong, W. Zhao, B.-W. Mao, X. Xu and L.-S. Zheng, One-step preparation of large-scale self-assembled monolayers of cyanuric acid and melamine supramolecular species on Au(111) surfaces, *J. Phys. Chem. C*, 2008, **112**, 4209–4218.

13 X. Zhang, T. Chen, Q. Chen, L. Wang and L.-J. Wan, Self-assembly and aggregation of melamine and melamine–uric/cyanuric acid investigated by STM and AFM on solid surfaces, *Phys. Chem. Chem. Phys.*, 2009, **11**, 7708–7712.

14 L. M. A. Perdigão, E. W. Perkins, J. Ma, P. A. Staniec, B. L. Rogers, N. R. Champness and P. H. Beton, Bimolecular networks and supramolecular traps on Au(111), *J. Phys. Chem. B*, 2006, **110**, 12539–12542.

15 L. Wang, H.-X. Shi, W.-Y. Wang, H. Shi and X. Shao, Identifying the Hydrogen bonding patterns of melamine and melem self-assemblies on Au(111) surface, *Acta Phys.-Chim. Sin.*, 2017, **33**, 393–398.

16 F. Silly, A. Q. Shaw, M. R. Castell, G. A. D. Briggs, M. Mura, N. Martsinovich and L. Kantorovich, Melamine structures on the Au(111) surface, *J. Phys. Chem. C*, 2008, **112**, 11476–11480.
17 C. H. Schmitz, J. Ikonomov and M. Sokolowski, Two commensurate hydrogen-bonded monolayer structures of melamine on Ag(111), *Surf. Sci.*, 2011, **605**, 1–6.
18 C. Wang, R. F. de Oliveira, K. Jiang, Y. Zhao, N. Turetta, C. Ma, B. Han, H. Zhang, D. Tranca, X. Zhuang, L. Chi, A. Ciesielski and P. Samorì, Boosting the electronic and catalytic properties of 2D semiconductors with supramolecular 2D hydrogen-bonded superlattices, *Nat. Commun.*, 2022, **13**, 510.
19 M. Shalom, S. Inal, C. Fettkenhauer, D. Neher and M. Antonietti, Improving Carbon Nitride Photocatalysis by Supramolecular Preorganization of Monomers, *J. Am. Chem. Soc.*, 2013, **135**, 7118–7121.
20 V. V. Korolkov, M. Baldoni, K. Watanabe, T. Taniguchi, E. Besley and P. H. Beton, Supramolecular heterostructures formed by sequential epitaxial deposition of two-dimensional hydrogen-bonded arrays, *Nat. Chem.*, 2017, **9**, 1191–1197.
21 J. Wu, P. P. Bag, Y. Xu, L. Gong, C. He, X. Chen and J. Zhang, Graphene-Like Hydrogen-Bonded Melamine–Cyanuric Acid Supramolecular Nanosheets as Pseudo-Porous Catalyst Support, *Adv. Mater.*, 2021, **33**, e2007368.
22 Z. Liu, K. Sun, X. Li, L. Li, H. Zhang and L. Chi, Electronic Decoupling of Organic Layers by a Self-Assembled Supramolecular Network on Au(111), *J. Phys. Chem. Lett.*, 2019, **10**, 4297–4302.
23 P. A. Staniec, L. M. A. Perdigão, B. L. Rogers, N. R. Champness and P. H. Beton, Honeycomb networks and chiral superstructures formed by cyanuric acid and melamine on Au(111), *J. Phys. Chem. C*, 2007, **111**, 886–893.
24 J. A. Theobald, N. S. Oxtoby, M. A. Phillips, N. R. Champness and P. H. Beton, Controlling molecular deposition and layer structure with supramolecular surface assemblies, *Nature*, 2003, **424**, 1029–1031.
25 J. C. Swarbrick, B. L. Rogers, N. R. Champness and P. H. Beton, Hydrogen-bonded PTCDA-melamine networks and mixed phases, *J. Phys. Chem. B*, 2006, **110**, 6110–6114.
26 C.-A. Palma, J. Bjork, M. Bonini, M. S. Dyer, A. Llanes-Pallas, D. Bonifazi, M. Persson and P. Samorì, Tailoring Bicomponent Supramolecular Nanoporous Networks: Phase Segregation, Polymorphism, and Glasses at the Solid–Liquid Interface, *J. Am. Chem. Soc.*, 2009, **131**, 13062–13071.
27 L. M. A. Perdigão, G. N. Fontes, B. L. Rogers, N. S. Oxtoby, G. Goretzki, N. R. Champness and P. H. Beton, Coadsorbed NTCDI-melamine mixed phases on Ag–Si(111), *Phys. Rev. B: Condens. Matter Mater. Phys.*, 2007, **76**, 245402.
28 Q. Liang, B. Shao, S. Tong, Z. Liu, L. Tang, Y. Liu, M. Cheng, Q. He, T. Wu, Y. Pan, J. Huang and Z. Peng, Recent advances of melamine self-assembled graphitic carbon nitride-based materials: design, synthesis and application in energy and environment, *Chem. Eng. J.*, 2021, **405**, 126951.
29 E. Arunan, G. R. Desiraju, R. A. Klein, J. Sadlej, S. Scheiner, I. Alkorta, D. C. Clary, R. H. Crabtree, J. J. Dannenberg, P. Hobza, H. G. Kjaergaard, A. C. Legon, B. Mennucci and D. J. Nesbitt, Definition of the hydrogen bond (IUPAC Recommendations 2011), *Pure Appl. Chem.*, 2011, **83**, 1637–1641.
30 T. Steiner, The Hydrogen Bond in the Solid State, *Angew. Chem., Int. Ed.*, 2002, **41**, 48–76.
31 S. J. Grabowski, Hydrogen bond types which do not fit accepted definitions, *Chem. Commun.*, 2024, **60**, 6239–6255.
32 G. N. Pairas and P. G. Tsoungas, H-Bond: The Chemistry-Biology H-Bridge, *Chem. Select Rev.*, 2016, **1**, 4520–4532.
33 E. Arunan, G. R. Desiraju, R. A. Klein, J. Sadlej, S. Scheiner, I. Alkorta, D. C. Clary, R. H. Crabtree, J. J. Dannenberg, P. Hobza, H. G. Kjaergaard, A. C. Legon, B. Mennucci and D. J. Nesbitt, Defining the hydrogen bond: an account (IUPAC Technical Report), *Pure Appl. Chem.*, 2011, **83**, 1619–1636.
34 P. A. Hunt, C. R. Ashworth and R. P. Matthews, Hydrogen bonding in ionic liquids, *Chem. Soc. Rev.*, 2015, **44**, 1257–1288.
35 J. J. Novo, A. Mota and E. D'Oria, in *Hydrogen Bonding—New Insights*, ed. S. J. Grabowski, Springer, 2006, pp. 193–244.
36 S. Garcia-Gil, A. Arnau and A. Garcia-Lekue, Exploring large O 1s and N 1s core level shifts due to intermolecular hydrogen bond formation in organic molecules, *Surf. Sci.*, 2013, **613**, 102–107.
37 V. Lanzilotto, J. L. Silva, T. Zhang, M. Stredansky, C. Grazioli, K. Simonov, E. Giangrisostomi, R. Ovsyannikov, M. D. Simone, M. Coreno, C. M. Araujo, B. Brena and C. Puglia, Spectroscopic fingerprints of intermolecular H-bonding interactions in carbon nitride model compounds, *Chem. – Eur. J.*, 2018, **24**, 14198–14206.
38 A. Ponzi, M. Rosa, G. Kladnik, I. Unger, A. Ciavardini, L. D. Nardi, E. Viola, C. Nicolas, N. Došlić, A. Goldoni and V. Lanzilotto, Inequivalent Solvation Effects on the N 1s Levels of Self-Associated Melamine Molecules in Aqueous Solution, *J. Phys. Chem. B*, 2023, **127**, 3016–3025.
39 G. Fronzoni, A. Cossaro, R. Costantini, L. D. Nardi, E. Viola, G. Balducci, V. Lanzilotto and D. Toffoli, Core-level spectroscopic probing of the heteromolecular H-bonding interaction in cyanuric Acid/Melamine 2D networks, *Appl. Surf. Sci.*, 2024, **642**, 158573.
40 D. Toffoli, R. Costantini, E. Bernes, L. D. Nardi, G. Balducci, E. Viola, G. Fronzoni, A. Cossaro and V. Lanzilotto, Inter- and intra-molecular charge redistributions in H-bonded Cyanuric Acid*Melamine (CA*M) networks: insight from core level spectroscopy and natural bond orbital analysis, *Chem. – Eur. J.*, 2024, e202403782.
41 A. Nilsson, H. Ogasawara, M. Cavalleri, D. Nordlund, M. Nyberg, Ph Wernet and L. G. M. Pettersson, The hydrogen bond in ice probed by soft X-ray spectroscopy and density functional theory, *J. Chem. Phys.*, 2005, **122**, 154505.
42 M. Cavalleri, H. Ogasawara, L. G. M. Pettersson and A. Nilsson, The interpretation of X-ray absorption spectra of water and ice, *Chem. Phys. Lett.*, 2002, **364**, 363–370.

43 V. Lanzilotto, D. Toffoli, E. Bernes, M. Stener, E. Viola, A. Cossaro, R. Costantini, C. Grazioli, R. Totani and G. Fronzoni, Probing Intermolecular H-Bonding Interactions in Cyanuric Acid Networks: Quenching of the N K-Edge Sigma Resonances, *J. Phys. Chem.*, 2022, **126**, 6870–6881.

44 K. Patkowski, Recent developments in symmetry-adapted perturbation theory, *Wiley Interdiscip. Rev.: Comput. Mol. Sci.*, 2020, **10**, e1452.

45 K. Szalewicz, Symmetry-adapted perturbation theory of intermolecular forces, *Wiley Interdiscip. Rev.: Comput. Mol. Sci.*, 2012, **2**, 254–272.

46 K. Kitaura and K. Morokuma, A new energy decomposition scheme for molecular interactions within the Hartree–Fock approximation, *Int. J. Quantum Chem.*, 1976, **10**, 325–340.

47 T. K. Ghanty, V. N. Staroverov, P. R. Koren and E. R. Davidson, Is the Hydrogen Bond in Water Dimer and Ice Covalent?, *J. Am. Chem. Soc.*, 2000, **122**, 1210–1214.

48 E. D. Glendening and A. Streitwieser, Natural energy decomposition analysis: An energy partitioning procedure for molecular interactions with application to weak hydrogen bonding, strong ionic, and moderate donor–acceptor interactions, *J. Chem. Phys.*, 1994, **100**, 2900–2909.

49 W. J. Stevens and W. H. Fink, Frozen fragment reduced variational space analysis of hydrogen bonding interactions. Application to the water dimer, *Chem. Phys. Lett.*, 1987, **139**, 15–22.

50 P. S. Bagus, K. Hermann and C. W. Bauschlicher, A new analysis of charge transfer and polarization for ligand–metal bonding: Model studies of Al_4CO and Al_4NH_3, *J. Chem. Phys.*, 1984, **80**, 4378–4386.

51 R. J. Azar and M. Head-Gordon, An energy decomposition analysis for intermolecular interactions from an absolutely localized molecular orbital reference at the coupled-cluster singles and doubles level, *J. Chem. Phys.*, 2012, **136**, 024103.

52 A. J. Misquitta, Charge Transfer from Regularized Symmetry-Adapted Perturbation Theory, *J. Chem. Theory Comput.*, 2013, **9**, 5313–5326.

53 A. J. Stone and A. J. Misquitta, Charge-transfer in Symmetry-Adapted Perturbation Theory, *Chem. Phys. Lett.*, 2009, **473**, 201–205.

54 T. Clark, J. S. Murray and P. Politzer, Role of Polarization in Halogen Bonds, *Aust. J. Chem.*, 2013, **67**, 451–456.

55 M. Hennemann, J. S. Murray, P. Politzer, K. E. Riley and T. Clark, Polarization-induced σ-holes and hydrogen bonding, *J. Mol. Model.*, 2012, **18**, 2461–2469.

56 P. Politzer, J. S. Murray and T. Clark, Mathematical modeling and physical reality in noncovalent interactions, *J. Mol. Model.*, 2015, **21**, 52.

57 F. Weinhold, Nature of H-bonding in clusters, liquids, and enzymes: an ab initio, natural bond orbital perspective, *THEOCHEM*, 1997, **398**, 181–197.

58 F. Weinhold, Resonance Character of Hydrogen-bonding Interactions in Water and Other H-bonded Species, *Adv. Protein Chem.*, 2005, **72**, 121–155.

59 J. P. Foster and F. Weinhold, Natural hybrid orbitals, *J. Am. Chem. Soc.*, 1980, **102**, 7211–7218.

60 J. R. Lane, J. Contreras-García, J.-P. Piquemal, B. J. Miller and H. G. Kjaergaard, Are Bond Critical Points Really Critical for Hydrogen Bonding?, *J. Chem. Theory Comput.*, 2013, **9**, 3263–3266.

61 C. F. Matta and R. J. Boyd, in *The Quantum Theory of Atoms in Molecules*, ed. C. F. Matta and R. J. Boyd, WILEY-VCH Verlag GmbH & Co. KGaA, Weinheim, 2007.

62 R. E. A. Kelly, Y. J. Lee and L. N. Kantorovich, Homopairing Possibilities of the DNA Base Adenine, *J. Phys. Chem. B*, 2005, **109**, 11933–11939.

63 R. E. A. Kelly and L. N. Kantorovich, Homopairing Possibilities of the DNA Base Thymine and the RNA Base Uracil: An ab Initio Density Functional Theory Study, *J. Phys. Chem. B*, 2006, **110**, 2249–2255.

64 R. E. A. Kelly, Y. J. Lee and L. N. Kantorovich, Homopairing Possibilities of the DNA Bases Cytosine and Guanine: An ab Initio DFT Study, *J. Phys. Chem. B*, 2005, **109**, 22045–22052.

65 R. E. A. Kelly and L. N. Kantorovich, Homopairings of the Artificial Nucleobase 1H-Benzoimidazole-4,7-dione, *J. Phys. Chem. B*, 2009, **113**, 16016–16020.

66 R. Otero, M. Lukas, R. E. A. Kelly, W. Xu, E. Lægsgaard, I. Stensgaard, L. N. Kantorovich and F. Besenbacher, Elementary Structural Motifs in a Random Network of Cytosine Adsorbed on a Gold(111) Surface, *Science*, 2008, **319**, 312–315.

67 D. Nordlund, M. Odelius, H. Bluhm, H. Ogasawara, L. G. M. Pettersson and A. Nilsson, Electronic structure effects in liquid water studied by photoelectron spectroscopy and density functional theory, *Chem. Phys. Lett.*, 2008, **460**, 86–92.

68 Ph Wernet, D. Nordlund, U. Bergmann, M. Cavalleri, M. Odelius, H. Ogasawara, L. A. Näslund, T. K. Hirsch, L. Ojamäe, P. Glatzel, L. G. M. Pettersson and A. Nilsson, The Structure of the First Coordination Shell in Liquid Water, *Science*, 2004, **304**, 995–999.

69 J. N. O'Shea, Y. Luo, J. Schnadt, L. Patthey, H. Hillesheimer, J. Krempasky, D. Nordlund, M. Nagasono, P. A. Bruhwiler and N. Mårtensson, Hydrogen-bond induced surface core-level shift in pyridinecarboxylic acids, *Surf. Sci.*, 2001, **486**, 157–166.

70 J. S. Stevens, L. K. Newton, C. Jaye, C. A. Muryn, D. A. Fischer and S. L. M. Schroeder, Proton Transfer, Hydrogen Bonding, and Disorder: Nitrogen Near-Edge X-ray Absorption Fine Structure and X-ray Photoelectron Spectroscopy of Bipyridine–Acid Salts and Co-crystals, *Cryst. Growth Des.*, 2015, **15**, 1776–1783.

71 J. S. Stevens, S. Coultas, C. Jaye, D. A. Fischer and S. L. M. Schroeder, Core level spectroscopies locate hydrogen in the proton transfer pathway – identifying quasi-symmetrical hydrogen bonds in the solid state, *Phys. Chem. Chem. Phys.*, 2020, **22**, 4916–4923.

72 A. Ugolotti, V. Lanzilotto, C. Grazioli, L. Schio, J. M. Zamalloa-Serrano, M. Stredansky, T. Zhang, M. de Simone, L. Ferraro, L. Floreano, M. Coreno, C. Puglia and

C. D. Valentin, In-Plane Hydrogen Bonds and Out-of-Plane Dipolar Interactions in Self-Assembled Melem Networks, *J. Phys. Chem. C*, 2023, **127**, 11307–11316.
73 G. Balducci, M. Romeo, M. Stener, G. Fronzoni, D. Cvetko, A. Cossaro, M. Dell'Angela, G. Kladnik, L. Venkataraman and A. Morgante, Computational Study of Amino Mediated Molecular Interaction Evidenced in N 1s NEXAFS: 1,4-Diaminobenzene on Au(111), *J. Phys. Chem. C*, 2015, **119**, 1988–1995.
74 C. F. Guerra, F. M. Bickelhaupt, J. G. Snijders and E. J. Baerends, The nature of the Hydrogen bond in DNA base pairs: the role of charge transfer and resonance assistance, *Chem. – Eur. J.*, 1999, **5**, 3581–3594.
75 C. F. Guerra and F. M. Bickelhaupt, Orbital interactions in strong and weak Hydrogen bonds are essential for DNA replication, *Angew. Chem., Int. Ed.*, 2002, **41**, 2092–2095.
76 B. Wang, W. Jiang, X. Dai, Y. Gao, Z. Wang and R.-Q. Zhang, Molecular orbital analysis of the hydrogen bonded water dimer, *Sci. Rep.*, 2016, **6**, 22099.
77 Z. Zhang, W. Jiang, B. Wang and Z. Wang, Quantitative contribution of molecular orbitals to hydrogen bonding in a water dimer: Electron density projected integral (EDPI) analysis, *Chem. Phys. Lett.*, 2017, **678**, 98–101.
78 J. P. Perdew, K. Burke and M. Ernzerhof, Generalized Gradient Approximation Made Simple, *Phys. Rev. Lett.*, 1996, **77**, 3865–3868.
79 J. P. Perdew, K. Burke and M. Ernzerhof, Generalized Gradient Approximation Made Simple [Phys. Rev. Lett. 77, 3865 (1996)], *Phys. Rev. Lett.*, 1996, **78**, 1396.
80 G. Kresse and J. Hafner, Ab initio molecular dynamics for liquid metals, *Phys. Rev. B: Condens. Matter Mater. Phys.*, 1993, **47**, 558–561.
81 G. Kresse and J. Hafner, Ab initio molecular-dynamics simulation of the liquid-metal–amorphous-semiconductor transition in germanium, *Phys. Rev. B: Condens. Matter Mater. Phys.*, 1994, **49**, 14251–14269.
82 G. Kresse and J. Furthmüller, Efficiency of ab-initio total energy calculations for metals and semiconductors using a plane-wave basis set, *Comput. Mater. Sci.*, 1996, **6**, 15–50.
83 G. Kresse and J. Furthmüller, Efficient iterative schemes for ab initio total-energy calculations using a plane-wave basis set, *Phys. Rev. B: Condens. Matter Mater. Phys.*, 1996, **54**, 11169–11186.
84 S. Grimme, J. Antony, S. Ehrlich and H. Krieg, A consistent and accurate ab initio parametrization of density functional dispersion correction (DFT-D) for the 94 elements H-Pu, *J. Chem. Phys.*, 2010, **132**, 154104.
85 R. L. H. Freire, D. Guedes-Sobrinho, A. Kiejna and J. L. F. D. Silva, Comparison of the Performance of van der Waals Dispersion Functionals in the Description of Water and Ethanol on Transition Metal Surfaces, *J. Phys. Chem. C*, 2018, **122**, 1577–1588.
86 J. Ireta, J. Neugebauer and M. Scheffler, On the Accuracy of DFT for Describing Hydrogen Bonds: Dependence on the Bond Directionality, *J. Phys. Chem. A*, 2004, **108**, 5692–5698.
87 S. Refaely-Abramson, S. Sharifzadeh, N. Govind, J. Autschbach, J. B. Neaton, R. Baer and L. Kronik, Quasiparticle Spectra from a Nonempirical Optimally Tuned Range-Separated Hybrid Density Functional, *Phys. Rev. Lett.*, 2012, **109**, 226405.
88 L. Kronik, T. Stein, S. Refaely-Abramson and R. Baer, Excitation Gaps of Finite-Sized Systems from Optimally Tuned Range-Separated Hybrid Functionals, *J. Chem. Theory Comput.*, 2012, **8**, 1515–1531.
89 J. M. Skelton, D. S. D. Gunn, S. Metz and S. C. Parker, Accuracy of Hybrid Functionals with Non-Self-Consistent Kohn–Sham Orbitals for Predicting the Properties of Semiconductors, *J. Chem. Theory Comput.*, 2020, **16**, 3543–3557.
90 A. J. Garza and G. E. Scuseria, Predicting Band Gaps with Hybrid Density Functionals, *J. Phys. Chem. Lett.*, 2016, **7**, 4165–4170.
91 M. Mura, N. Martsinovich and L. Kantorovich, Theoretical study of melamine superstructures and their interaction with the Au(111) surface, *Nanotechnology*, 2008, **19**, 465704.
92 J. Heyd and G. E. Scuseria, Assessment and validation of a screened Coulomb hybrid density functional, *J. Chem. Phys.*, 2004, **120**, 7274–7280.
93 J. Heyd and G. E. Scuseria, Efficient hybrid density functional calculations in solids: Assessment of the Heyd–Scuseria–Ernzerhof screened Coulomb hybrid functional, *J. Chem. Phys.*, 2004, **121**, 1187–1192.
94 J. Heyd, J. E. Peralta, G. E. Scuseria and R. L. Martin, Energy band gaps and lattice parameters evaluated with the Heyd-Scuseria-Ernzerhof screened hybrid functional, *J. Chem. Phys.*, 2005, **123**, 174101.
95 A. F. Izmaylov, G. E. Scuseria and M. J. Frisch, Efficient evaluation of short-range Hartree-Fock exchange in large molecules and periodic systems, *J. Chem. Phys.*, 2006, **125**, 104103.
96 J. Heyd, G. E. Scuseria and M. Ernzerhof, Erratum: ''Hybrid functionals based on a screened Coulomb potential'' [J. Chem. Phys. 118, 8207 (2003)], *J. Chem. Phys.*, 2006, **124**, 219906.
97 A. V. Krukau, O. A. Vydrov, A. F. Izmaylov and G. E. Scuseria, Influence of the exchange screening parameter on the performance of screened hybrid functionals, *J. Chem. Phys.*, 2006, **125**, 224106.
98 T. M. Henderson, A. F. Izmaylov, G. Scalmani and G. E. Scuseria, Can short-range hybrids describe long-range-dependent properties?, *J. Chem. Phys.*, 2009, **131**, 044108.
99 T. H. Dunning, Gaussian basis sets for use in correlated molecular calculations. I. The atoms boron through neon and hydrogen, *J. Chem. Phys.*, 1989, **90**, 1007–1023.
100 J. M. Turney, A. C. Simmonett, R. M. Parrish, E. G. Hohenstein, F. A. Evangelista, J. T. Fermann, B. J. Mintz, L. A. Burns, J. J. Wilke, M. L. Abrams, N. J. Russ, M. L. Leininger, C. L. Janssen, E. T. Seidl, W. D. Allen, H. F. Schaefer, R. A. King, E. F. Valeev, C. D. Sherrill and T. D. Crawford, Psi4: an open-source ab initio electronic structure program, *Wiley Interdiscip. Rev.: Comput. Mol. Sci.*, 2012, **2**, 556–565.

101 P. Ros and G. C. A. Schuit, Molecular Orbital Calculations on Copper Chloride Complexes, *Theor. Chim. Acta*, 1966, **4**, 1–12.
102 S. I. Gorelsky and A. B. P. Lever, Electronic structure and spectra of ruthenium diimine complexes by density functional theory and INDO/S. Comparison of the two methods, *J. Organomet. Chem.*, 2001, **635**, 187–196.
103 C. Ehlert and T. Klamroth, PSIXAS: a Psi4 plugin for efficient simulations of X-ray absorption spectra based on the transition-potential and Δ-Kohn–Sham method, *J. Comput. Chem.*, 2020, **41**, 1781–1789.
104 I. E. Brumboiu and T. Fransson, Core–hole delocalization for modeling x-ray spectroscopies: a cautionary tale, *J. Chem. Phys.*, 2022, **156**, 214109.
105 A. Bergner, M. Dolg, W. Küchle, H. Stoll and H. Preuß, Ab initio energy-adjusted pseudopotentials for elements of groups 13–17, *Mol. Phys.*, 1993, **80**, 1431–1441.
106 B. P. Pritchard, D. Altarawy, B. Didier, T. D. Gibson and T. L. Windus, New Basis Set Exchange: An Open, Up-to-Date Resource for the Molecular Sciences Community, *J. Chem. Inf. Model.*, 2019, **59**, 4814–4820.
107 D. E. Woon and T. H. Dunning, Gaussian basis sets for use in correlated molecular calculations. III. The atoms aluminum through argon, *J. Chem. Phys.*, 1993, **98**, 1358–1371.
108 R. A. Kendall, T. H. Dunning and R. J. Harrison, Electron affinities of the first-row atoms revisited. Systematic basis sets and wave functions, *J. Chem. Phys.*, 1992, **96**, 6796–6806.
109 G. Hermann, V. Pohl, J. C. Tremblay, B. Paulus, H. Hege and A. Schild, ORBKIT: a modular python toolbox for cross-platform postprocessing of quantum chemical wavefunction data, *J. Comput. Chem.*, 2016, **37**, 1511–1520.
110 Jmol: an open-source Java viewer for chemical structures in 3D, https://www.jmol.org/.
111 V. F. Scalfani, A. J. Williams, V. Tkachenko, K. Karapetyan, A. Pshenichnov, R. M. Hanson, J. M. Liddie and J. E. Bara, Programmatic conversion of crystal structures into 3D printable files using Jmol, *J. Cheminf.*, 2016, **8**, 66.
112 Blender 3.6 LTS, https://www.blender.org/download/lts/3-6/.
113 D. W. Turner, C. Baker, A. D. Baker and C. R. Brundle, *Molecular Photoelectron Spectroscopy: A Handbook of He 584 Å Spectra*, Wiley-Interscience, London/New York, 1970.

